Nuclear Instruments and Methods in Physics Research A 676 (2012) 54–65

Contents lists available at SciVerse ScienceDirect

Nuclear Instruments and Methods in Physics Research A

journal homepage: www.elsevier.com/locate/nima

New air fluorescence detectors employed in the Telescope Array experiment

H. Tokuno [a,*], Y. Tameda [b], M. Takeda [b], K. Kadota [c], D. Ikeda [b], M. Chikawa [d], T. Fujii [e], M. Fukushima [b,f], K. Honda [g], N. Inoue [h], F. Kakimoto [a], S. Kawana [h], E. Kido [b], J.N. Matthews [i], T. Nonaka [b], S. Ogio [e], S. Okuda [e], S. Ozawa [j], H. Sagawa [b], N. Sakurai [e], T. Shibata [b], A. Taketa [k], S.B. Thomas [i], T. Tomida [g], Y. Tsunesada [a], S. Udo [l], T. Abu-zayyad [i], R. Aida [g], M. Allen [i], R. Anderson [i], R. Azuma [a], E. Barcikowski [i], J.W. Belz [i], D.R. Bergman [i], S.A. Blake [i], R. Cady [i], B.G. Cheon [m], J. Chiba [n], E.J. Cho [m], W.R. Cho [o], H. Fujii [p], T. Fukuda [a], D. Gorbunov [q], W. Hanlon [i], K. Hayashi [a], Y. Hayashi [e], N. Hayashida [l], K. Hibino [l], K. Hiyama [b], T. Iguchi [a], K. Ikuta [g], T. Ishii [g], R. Ishimori [a], D. Ivanov [i,r], S. Iwamoto [g], C.C.H. Jui [i], O. Kalashev [q], T. Kanbe [g], K. Kasahara [j], H. Kawai [s], S. Kawakami [e], H.B. Kim [m], H.K. Kim [o], J.H. Kim [m], J.H. Kim [t], K. Kitamoto [d], K. Kobayashi [n], Y. Kobayashi [a], Y. Kondo [b], K. Kuramoto [e], V. Kuzmin [q], Y.J. Kwon [o], S.I. Lim [v], S. Machida [a], K. Martens [f], J. Martineau [i], T. Matsuda [p], T. Matsuura [a], T. Matsuyama [e], I. Myers [i], M. Minamino [e], K. Miyata [n], H. Miyauchi [e], Y. Murano [a], T. Nakamura [u], S.W. Nam [v], M. Ohnishi [b], H. Ohoka [b], K. Oki [b], D. Oku [g], A. Oshima [e], I.H. Park [v], M.S. Pshirkov [w], D. Rodriguez [i], S.Y. Roh [t], G. Rubtsov [q], D. Ryu [t], A.L. Sampson [i], L.M. Scott [r], P.D. Shah [i], F. Shibata [g], H. Shimodaira [b], B.K. Shin [m], J.I. Shin [o], T. Shirahama [h], J.D. Smith [i], P. Sokolsky [i], T.J. Sonley [i], R.W. Springer [i], B.T. Stokes [i], S.R. Stratton [i,r], T. Stroman [i], S. Suzuki [p], Y. Takahashi [b], M. Takita [b], H. Tanaka [e], K. Tanaka [x], M. Tanaka [p], G.B. Thomson [i], P. Tinyakov [q,w], I. Tkachev [q], S. Troitsky [q], K. Tsutsumi [a], Y. Tsuyuguchi [g], Y. Uchihori [y], H. Ukai [g], G. Vasiloff [i], Y. Wada [h], T. Wong [i], M. Wood [i], Y. Yamakawa [b], H. Yamaoka [p], K. Yamazaki [e], J. Yang [v], S. Yoshida [s], H. Yoshii [z], R. Zollinger [i], Z. Zundel [i]

[a] Tokyo Institute of Technology, Meguro, Tokyo, Japan
[b] Institute for Cosmic Ray Research, University of Tokyo, Kashiwa, Chiba, Japan
[c] Tokyo City University, Setagaya-ku, Tokyo, Japan
[d] Kinki University, Higashi Osaka, Osaka, Japan
[e] Osaka City University, Osaka, Osaka, Japan
[f] University of Tokyo, Institute for the Physics and Mathematics of the Universe, Kashiwa, Chiba, Japan
[g] University of Yamanashi, Interdisciplinary Graduate School of Medicine and Engineering, Kofu, Yamanashi, Japan
[h] Saitama University, Saitama, Saitama, Japan
[i] University of Utah, High Energy Astrophysics Institute, Salt Lake City, Utah, USA
[j] Waseda University, Advanced Research Institute for Science and Engineering, Shinjuku-ku, Tokyo, Japan
[k] Earthquake Research Institute, University of Tokyo, Bunkyo-ku, Tokyo, Japan
[l] Kanagawa University, Yokohama, Kanagawa, Japan
[m] Hanyang University, Seongdong-gu, Seoul, South Korea
[n] Tokyo University of Science, Noda, Chiba, Japan
[o] Yonsei University, Seodaemun-gu, Seoul, South Korea
[p] Institute of Particle and Nuclear Studies, KEK, Tsukuba, Ibaraki, Japan
[q] Institute for Nuclear Research of the Russian Academy of Sciences, Moscow, Russia
[r] Rutgers University, Piscataway, USA
[s] Chiba University, Chiba, Chiba, Japan
[t] Chungnam National University, Yuseong-gu, Daejeon, South Korea
[u] Kochi University, Kochi, Kochi, Japan
[v] Ewha Womans University, Seodaaemun-gu, Seoul, South Korea
[w] University Libre de Bruxelles, Brussels, Belgium
[x] Hiroshima City University, Hiroshima, Hiroshima, Japan
[y] National Institute of Radiological Science, Chiba, Chiba, Japan
[z] Ehime University, Matsuyama, Ehime, Japan

* Corresponding author. Tel.: +81 357342462; fax: +81 357342756.
E-mail address: htokuno@cr.phys.titech.ac.jp (H. Tokuno).

0168-9002/$ - see front matter
doi:10.1016/j.nima.2012.02.044

ARTICLE INFO

Article history:
Received 24 October 2011
Received in revised form
20 February 2012
Accepted 21 February 2012
Available online 3 March 2012

Keywords:
Ultra high energy cosmic rays
Extensive air showers
Air fluorescence light detectors

ABSTRACT

Since 2007, the Telescope Array (TA) experiment, based in Utah, USA, has been observing ultra high energy cosmic rays to understand their origins. The experiment includes a surface detector (SD) array and three fluorescence detector (FD) stations. The FD stations, installed surrounding the SD array, measure the air fluorescence light emitted from extensive air showers (EASs) for precise determination of their energies and species. The detectors employed at one of the three FD stations were relocated from the High Resolution Fly's Eye (HiRes) experiment. At the other two stations, newly designed detectors were constructed for the TA experiment. An FD consists of a primary mirror and a camera equipped with photomultiplier tube pixels. To obtain the EAS parameters with high accuracy, understanding the FD optical characteristics is important. In this paper, we report the characteristics and installation of the new FDs and the performances of the FD components. The results of the monitored mirror reflectance during the observation time are also described in this report.

1. Introduction

The Telescope Array project is a collaboration with 120 scientists from five nations (Japan, USA, Korea, Russia, and Belgium), with the observatory located in Utah, USA [1,2]. The detectors of the Telescope Array experiment include Surface Detectors (SDs) arranged in an array and Fluorescence Detector (FD) telescopes. Fig. 1 shows the detector map (squares: SD positions, triangles: FD station positions). The SD array consists of 507 SDs, arranged over an area of approximately 700 km^2 with 1.2 km spacing between the SDs [3]. The SDs measure the arrival timing and particle densities of Extensive Air Showers (EASs) using two-layered plastic scintillators of 3 m^2 area, and 1.2 cm thick. Three FD stations are placed at the perimeter of the SD array. The FDs measure the air fluorescence light emitted from EASs; the FD data are analyzed and the longitudinal development of EASs is reconstructed to estimate primary energies, arrival directions, and particle species with the aim of studying the nature of ultra high energy cosmic rays.

The FD station near the northwest corner of the SD array is composed of 14 FDs that were relocated from the High Resolution Fly's Eye (HiRes) experiment (e.g. [4]). For these FDs and for the data obtained using these FDs, we can use the same calibration and analysis methods used in the HiRes experiment [5]. The specifications, configurations, and calibrations of the relocated FDs can be obtained from previous reports on HiRes (e.g. [4]). On the other hand, the southeast (BRM) and southwest (LR) FD sites are composed of 12 FDs each. These FDs were newly designed for the TA experiment. A picture of the FD station is shown in Fig. 2.

An FD consists of a primary mirror and a photomultiplier tube (PMT) camera. We employed a spherical mirror to obtain a wide field of view (FOV) with a sufficient focusing power. In addition, the size of the collecting area of the mirror was determined from the maximum distance for detectable EASs at the highest energies. The mirror diameter and curvature radius were determined to be 3300 mm (area of 6.8 m^2) and 6067 mm, respectively. This setting realizes the detection of EASs with a sufficiently high accuracy from a distance of 30 km and with the primary energy of 10^{20} eV.

A primary mirror is composed of 18 hexagonal mirrors (called as mirror segments); the distance between the parallel sides of the mirror segment is 660 mm. A PMT camera consisting of 16×16 PMTs and having an effective area of 860 mm $\times$ 992 mm is set at a distance of 3000 mm from the mirror. The FOV of each PMT is approximately 1°, and that of the camera is 15° in elevation and 18° in azimuth. Fig. 3 shows a schematic view of the FD frame equipped with a pair of FDs, one each in the upper and lower parts of the frame. The heights of the upper and lower mirror centers and the upper and lower camera centers from the floor are 5.5, 1.5, 6.0, and

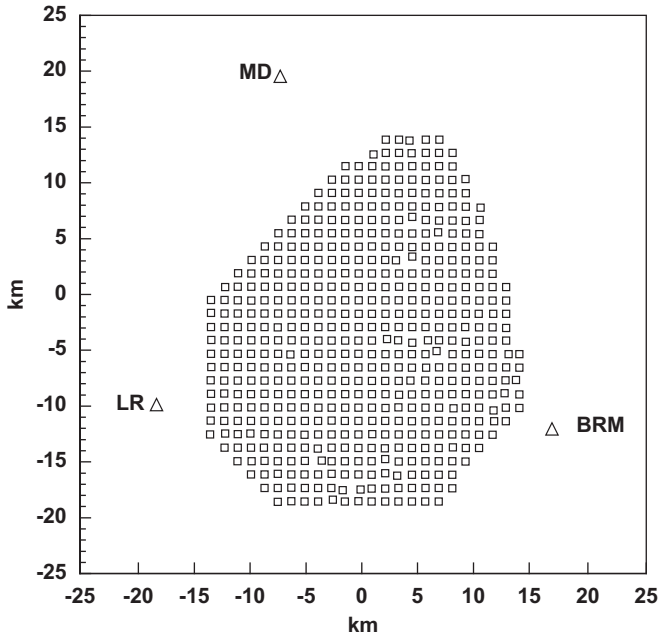

Fig. 1. Detector positions in the Telescope Array experiment. Squares: Surface Detectors (SDs), triangles: Fluorescence Detector telescope (FD) stations. SD array area: ~700 km^2, SD spacing: 1.2 km, and distance between FD stations: ~35 km.

Fig. 2. Picture showing the fluorescence detector station at Black Rock Mesa. Several FDs can be seen in the shutter openings.

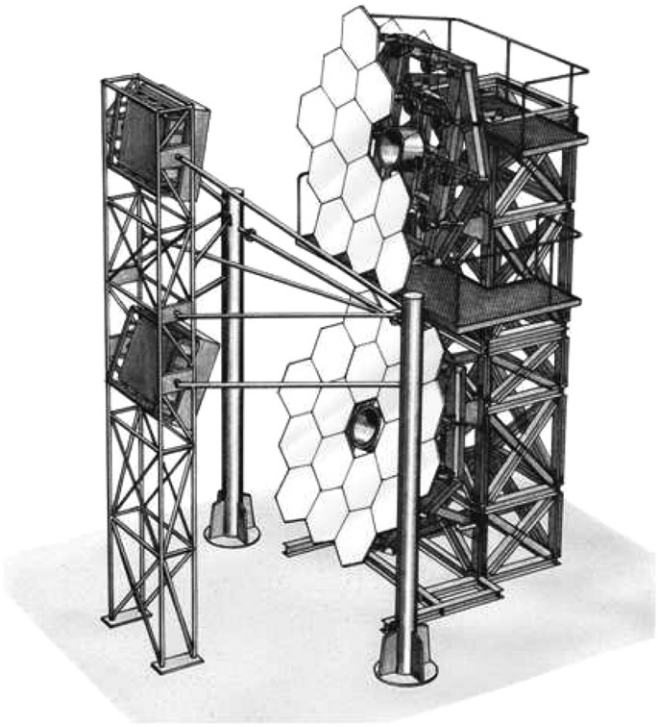

Fig. 3. Schematic view of the FDs. For visibility of mirror mounts, seven mirror segments are removed from the upper FD in this diagram. The upper FD views 3–18.5° above horizon and the lower FD views 17.5–33°.

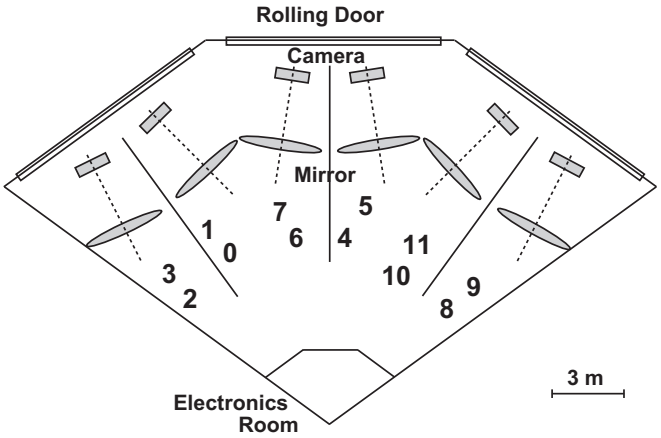

Fig. 4. Schematic projected view of the FD station projected onto the floor (solid lines: datum lines, dashed lines: azimuthal lines of each FD frame). The FDs are numbered according to their FOVs, as shown in this figure; the lower (upper) FDs have even (odd) numbers.

2.8 m, respectively. The FOV centers of the upper and lower FDs are at elevations of 10.5° and 25.5°, respectively. As shown in Fig. 3, no mirror segment is installed at the center of the primary mirror. During construction, a jig was mounted at this position for alignment of the optical system of the FD when it was constructed. Similarly, during normal operations, a UV light source called Xenon flasher is mounted here as a standard light source for the calibrations and adjustments of PMT gains [6]. The projected view of the FD station onto the station floor is shown in Fig. 4. The station has six FD frames; accordingly, the FOV of a station is from 3° to 33° in elevation and 108° in azimuth. The optical parameters of the FD are summarized in Table 1.

Using these FDs, we detect EASs and determine their parameters (i.e. the primary energy, the arrival direction, and the maximum

Table 1
The optical parameters for the FDs at BRM and LR. V: vertical, H: horizontal.

Mirror	
Diameter	3300 mm
Total area	6.8 m^2
Curvature	Spherical
Curvature radius	6067 mm
Camera	
Device	PMT (Hamamatsu R9508)
Dimension	860 mm (V) × 992 mm (H)
Number of pixel	16 × 16
FD	
Distance between camera and mirror	3000 mm
Spot size (diameter)	40 mm in which 68% of reflected photons fall
FOV/pixel	~1°
Total FOV/camera	18° (H) × 15.5° (V)
Obscuration ratio	25% (typical)
FD station	
Number of FD	12
Total FOV	33° (H) × 108° (V)

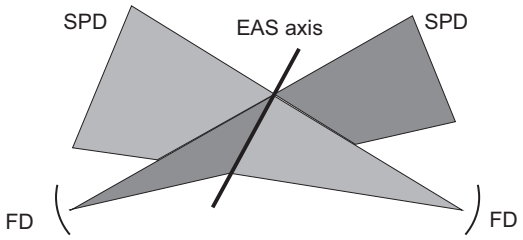

Fig. 5. Schematic view of the stereoscopic detection of a same EAS from two FD stations. At each FD station, a shower to detector plane (SDP) is obtained from a fitting using the pointing directions of the detected PMTs. The shower axis can be determined from the intersection of the two SDPs in the stereoscopic detection.

point of longitudinal development). Fig. 5 shows the schematic view of the stereoscopic detection of a same EAS from two FD stations. At each FD station, a shower to detector plane (SDP) is obtained from a fitting using the pointing directions of the detected PMTs. The shower axis can be determined from the intersection of the two SDPs in stereoscopic detection. Fig. 6 shows an event display of a typical observed EAS event by the FDs at BRM (in the right panel) and LR (in the left panel). The colored circles indicate PMTs which detected a significant signal, and the areas of circle indicate the measured light intensities. While colors indicate the arrival timing of the signal from each station trigger timing. Comparing these figures, the EAS track on the left panel is shorter and thicker than that on the right panel. These differences are caused by the different distances from EAS to FD. For this event, the distance of the reconstructed EAS from LR (the left panel) is nearer than that from BRM (the right panel). To reconstruct the EAS from the detected signals, an inverse Monte Carlo (IMC) method is employed. In the IMC, the detected signals are compared with simulated signals from EASs with varying sets of shower maximum point and shower size at that point. The parameter set which provides the best fit result is adopted as the most probable value of EAS parameters [7].

Requirements for measurement accuracies of shower parameters are summarized in Table 2. To ensure the accuracies of the parameters, studies of resolutions and systematic uncertainties of FD optics are important. Thus, we ensured that we accurately manufactured, constructed, and installed the FDs with utmost care and after confirmation of their optical characteristics.

In this paper, we describe the elements that constitute an FD and the installation process of the FDs. Moreover, the reflectance

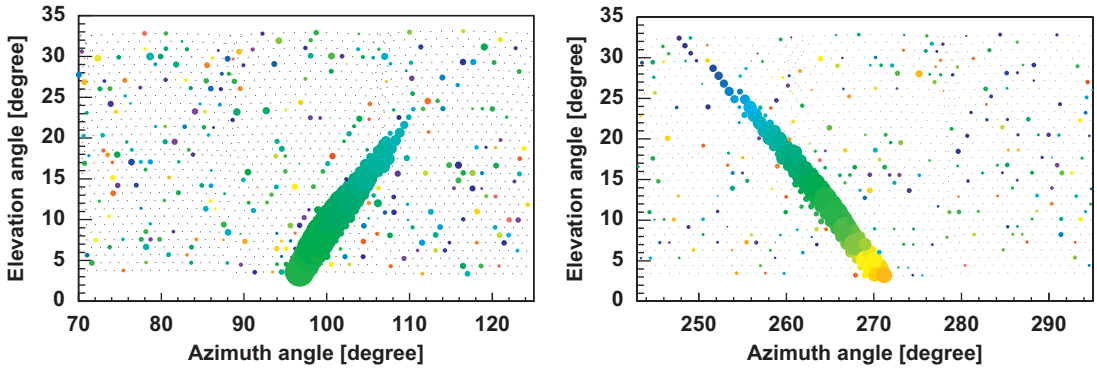

Fig. 6. Event display of a typical observed EAS event by the FDs at BRM (the right panel) and LR (the left panel). The colored circles indicate PMTs which had a significant signal, and the areas of circle are proportional to the light intensities. The color of the circle indicates the same arrival timing of the detected lights from each station trigger timing. (For interpretation of the references to color in this figure legend, the reader is referred to the web version of this article.)

Table 2
Requirements for the detection accuracies of observables for a stereo FD analysis.

Observable	Resolution	Uncertainty
Primary energy	10%	$<20\%$
Arrival direction	$<1^\circ$	$<1^\circ$
Shower maximum point	20 g/cm^2	<20 g/cm^2

of mirror segments, which are continuously monitored after installation, is also presented. The content of this paper is as follows. In Sections 2 and 3, we report the designs and productions of the PMT cameras and those of the mirror segments, respectively. Section 4 explains the installation of the cameras and mirrors. Mirror reflectance and its variations are described in Section 5.

2. Camera production

In this section, we describe the configuration of the newly designed PMT cameras and the results of user acceptance tests.

2.1. Photomultiplier tube

Each camera is composed of 256 PMTs. About 7000 PMTs including spares were produced. The PMT used in the TA experiment, Hamamatsu R9508 based on R6234-01 with a printed circuit board, is specially manufactured for the experiment. The photoelectric surface on the top of a tube is hexagonal in shape with a distance of 60 mm between the parallel sides; its effective area is equivalent to that of circle of 57 mm diameter (area: 25.3 cm^2) [6]. On the bottom of the tube, a printed circuit board which includes a bleeder and a preamplifier is installed. In order to reduce the contamination of the night sky background photons into fluorescence signals, we use a 4 mm thick optical filter (SCHOTT AG, BG3). The filter is mounted on the surface of each PMT using a self-fusing tape (Hitachi Chemical Co., Ltd., HIGHBON TAPE No. 2) and a polyimide film tape (3M, 5434). The transmittance of BG3 is greater than 80% in the wavelength range of 305–395 nm, which contains all of the major air fluorescence lines [6].

The PMTs were inspected by the supplier before shipping and were selected based on their cathode and anode sensitivities, dark current, and other basic parameters. In addition, the quantum efficiency (QE) in 270–750 nm with 10 nm step were measured for 32 sampled PMTs, and cathode uniformity on two orthogonal axis were measured for 300 sampled PMTs using a light source with 1 mm diameter spot. The results show that QE (e.g. $27.8\pm0.5\%$ at 350 nm) is consistent with their typical catalog values, and the measured uniformity is consistent with our measurement results [6].

After installation of camera, we adjusted the PMT gains relative to absolutely calibrated PMTs [8] and measured the uniformity of the PMT response at its photoelectric surface on the sites [6]. At the PMT gain adjustment, we imposed a required gain and low noise levels on PMTs. The required gain was 4×10^4 within the maximum applied high voltage of -1200 V.

During FD observations, each PMT gain is monitored every hour using Xenon flashers [6]. The typical light intensity of the Xe flasher is equivalent to 2×10^4 p.e./PMT per shot. This light intensity is approximately 100 times greater than the typical air fluorescence signals to give an accurate measurement with a small number of flasher shots (~10). We exchanged two of the 6144 PMTs installed, because these two PMTs showed a decrease in gain in the first half year. Since that time, no PMT has shown significant decrease in gain and no PMT has been exchanged. Detailed descriptions of the absolute PMT gain calibration and performance monitoring are presented elsewhere [6,8] and in a future paper.

2.2. Camera

The PMT camera is placed at the primary focus of each FD. Fig. 7 shows the schematic view of the PMT camera. The camera has a UV transparent acrylic window (KURARAY, PARAGLAS-UV00) attached in front of PMTs for protection from dust. The transmittance of the acrylic window is greater than 90% in the wavelength range of 300–400 nm [6]. PMTs were fixed on a 16 mm thick plate of extra super duralumin reference and were arranged on a triangular grid leaving a clearance gap of approximately 1 mm between them. The gap geometries were measured based on the uniformity of the camera surface response [6].

The DC power to the PMTs and signals from the PMTs are transferred through standard computing shielded category 5 LAN cables (length: 50–100 cm) between the PMTs and the patch panels inside a camera. The patch panels connected to the LAN cables are shown in Fig. 8. We use a shielded 40 core twisted pair cable (Bando Densen Co., Ltd., BIOS-A-2820P) to transfer the PMT signals for each of the 16 PMTs from the patch panels in a camera to a data acquisition (DAQ) system in the temperature controlled electronics room, situated 20 m from the camera location. The cable length for the upper and lower cameras is 25.5 m and 22.3 m, respectively.

The transferred PMT signals are received by a Signal Digitizer and Finder (SDF) module. The signals are digitized by a 12-bit, 40 MHz Flash ADC with the maximum voltage 2 V in SDF. To extend the dynamic range of readout signals, four consecutive digitization signals are summed. A SDF module has a 16 input channels, and 16 SDFs installed for each FD. From the digitized

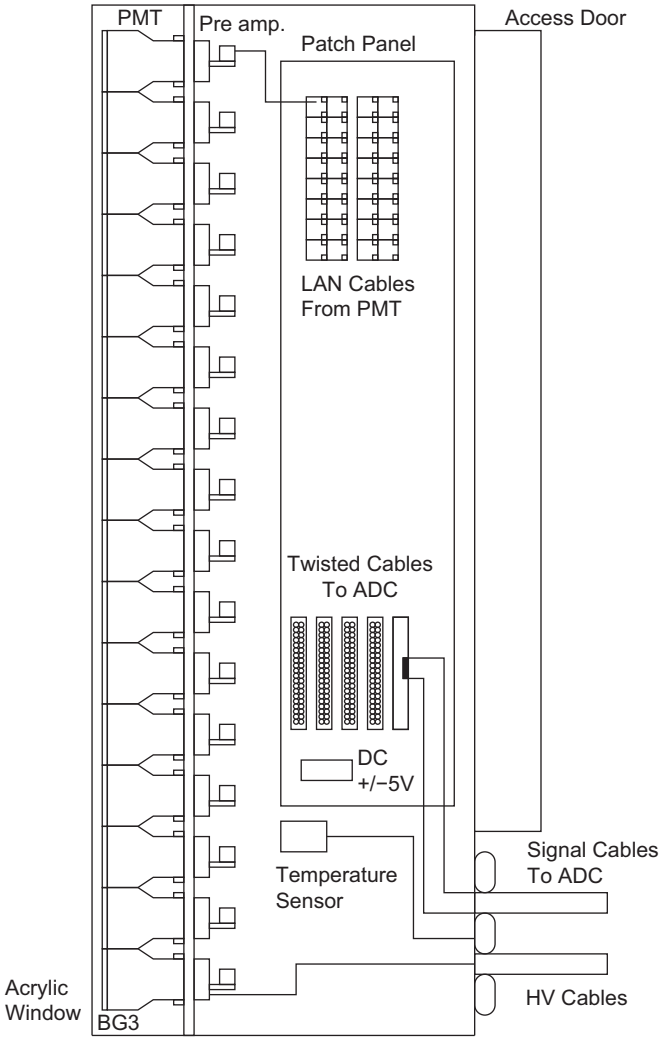

Fig. 7. Schematic side view of a PMT camera. Inside the camera, there are 256 PMTs, connected with signal and HV cables, and a temperature sensor.

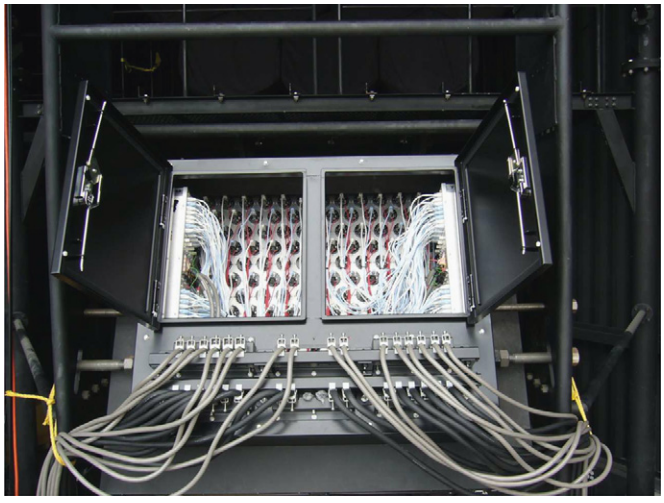

Fig. 8. Rear view of the PMT camera. In this photo, the rear doors to the camera have been opened to expose the wiring and other details.

SDF signals, a Track Finder (TF) module searches for EAS tracks. The operation clock in each module is synchronized with a central timing and trigger distributor (CTD) module. The CTD module also makes a trigger decision using information from TFs, and distributes a coincidence signal to SDFs. When trigger signal is distributed from CTD, all SDFs record a waveform with a time window (51.2 μs) to hard disk of personal computer. Using the CTD module, each FD station operates with independent triggers. Detailed descriptions of the electronics, DAQ system and trigger diagram are presented elsewhere [9,10].

High voltage (HV) is applied to each PMT via coaxial cables (Bando Densen Co., Ltd., 1.5D-2V) using a custom-made power supply (Takasago Co., Ltd.). The HV supply provides 256 outputs, and the HV value on each output can be controlled and monitored separately through Ethernet, with an absolute accuracy of $\pm 0.2\%$. This uncertainty corresponds to approximately $\pm 2\%$ of the PMT gains under our setting. The typical HV applied to the PMTs is -880 V, and the rated maximum voltage of HV supply is -1200 V. As a safety measure to protect human beings, PMTs, and the HV supply, the HV supply is automatically shut down when unusually high voltage or current are detected.

A DC power supply (KENWOOD, PW18-3AD) is connected to two patch panels to distribute DC voltage of ± 5 V to the 256 preamplifiers of a single camera.

3. Mirror segments and their production

In this section, we describe the specifications of the mirror segments employed in the new FDs of the TA experiment, their pre-shipment and acceptance inspections, and the inspection results.

3.1. Mirror segments

The 3.3 m aperture spherical mirror of the FD is composed of 18 smaller mirrors, as shown in Fig. 3. The mirror begins with borosilicate glass (SCHOTT AG, TEMPAX). Each segment is hexagonal in shape with a thickness of 10.5 mm and a distance of 660 mm between the parallel sides. An aluminum coating, 200 nm in thickness, was vacuum deposited onto the glass and a 50 nm layer was anodized to form a protective coating of Al_2O_3. The thickness of the anodization was to obtain the maximum reflectance at wavelength of 350 nm.

The demands upon the optical parameters and fabrication accuracies of mirror segments depend on the experimental requirement. In order to optimize the optical parameters, we studied the reconstruction accuracies of EASs using ray-tracing, EAS simulation, and reconstruction programs. From our studies, we determined the specifications of the optical parameters and the fabrication accuracies; the radius of curvature of the segment mirror was 6067 ± 100 mm, the spot size at the focal point was smaller than 40 mm diameter (it is comparable in size to the PMT surface), and the reflectance in the wavelength range of 300–400 nm was greater than 85%. The spot size on a camera edge is approximately two times larger than that on the camera center in our optical setting.

3.2. Mirror segment production

The segment mirror were manufactured (Sanko Seikohjyo Co., Ltd.) between January and November 2004, for the BRM station and between March and December 2006, for the LR station. In all, 500 segment mirrors, including spares, were produced. The procedure for mirror production is as follows. First, the mirror segment was shaped by heating a planar glass on a ceramic model plate in a temperature-controlled electric oven. After this, the mirrors were selected by curvature radius measurement. Next, the mirror surface was coated with 200 nm thick aluminum through the vacuum deposition. To protect the surface, 50 nm thick crystal layer was anodized to form Al_2O_3. These Al_2O_3 crystals were produced by

submerging the aluminized mirror in a solution containing ammonium hydroxide, tartaric acid, and ethylene glycol and applying a bias voltage. After the surface fabrication, the mirrors were selected based on reflectance measurement. Finally, a 150 mm diameter support disk made of the same borosilicate material as the mirror and a stainless steel flange were bonded to the back of the mirror using glue (3M, Dymax 840). The flange is used to support the mirror segment from the FD frame.

3.3. Acceptance test for curvature radius and spot size

The acceptance inspections included measurement of the curvature radius and spot size at the curvature center. From our ray-tracing studies, we estimated an acceptable spot diameter of 20 mm, in which 90% of the reflected photons fall at the center of the curvature. Because of this phenomenon, parallel incident light makes a spot of 40 mm diameter on the camera, in which 68% of reflected photons fall, as in the case of normal FD observation. We developed a test system to measure the curvature radius of mirrors as the distance corresponding to the minimum spot size. Fig. 9 shows a schematic view of the system, and Fig. 10 shows a photograph of the same. This system consisted of a linear precision motion stage (range: ± 250 mm, accuracy: 0.04 mm, Chuo Precision Industrial Co., Ltd., MM STAGE ALS-250-C2P with controller QT-CD1); a diffused light source, i.e. a green laser (wavelength: 532 nm, Kochi Toyonaka Giken Co., Ltd., GLM-D2) with a diffuser plate; an image scanner (range: 16 bit, resolution: 2400–4800 dpi, Canon, CanoScan LiDE80); and a laser distance meter (accuracy: ± 1 mm, Murakami Giken, DIST pro[4]a). The diffused light source was set 100 mm away from the optical axis of the mirror, and the center of the scanner's sensitive area was fixed at the axisymmetrical point to the optical axis. Both the light source and the scanner were mounted on the motion stage and were collectively moved between 6067 ± 100 mm from the center of the mirror in 5 mm steps. Next, we determined the curvature radius by searching for the point where the spot size was minimized. From our ray-tracing calculations, we confirmed that the spot size of the light reflected onto the scanner was minimized at the same distance as the curvature radius in spite of the off-axis alignments of the light source and the scanner.

A typical observed spot image is shown in Fig. 11. In this analysis, the image size was defined as the diameter of the circle

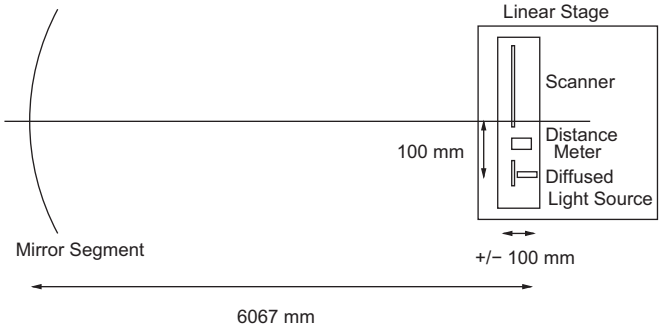

Fig. 9. Schematic diagram showing the setup for the measurement of curvature radius of mirror segment.

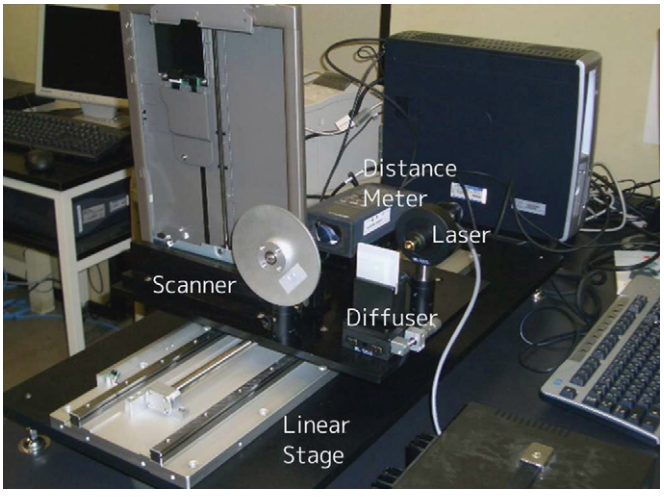

Fig. 10. Photograph of the equipment for measuring the curvature radius of mirror segment. This equipment includes a scanner, a distance meter, and a laser source with a diffuser plate, placed to the right on the linear stage.

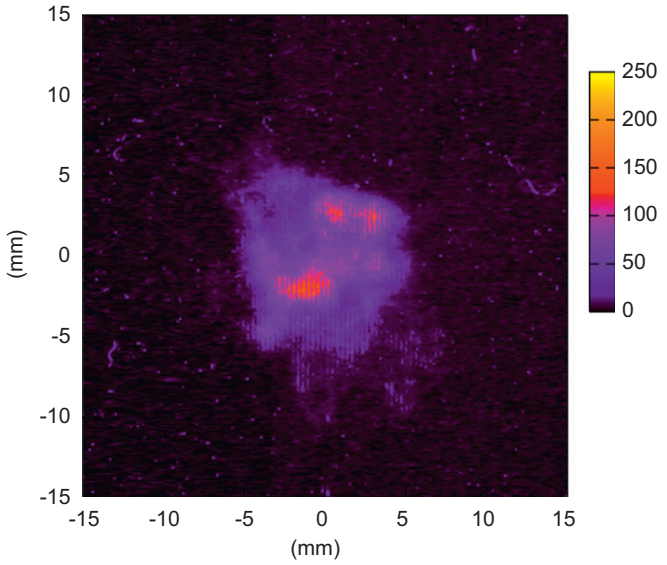

Fig. 11. Scanned image of reflected light at the distance equal to the curvature radius of the mirror. Colors show intensities of light in the electrical article. (For interpretation of the references to color in this figure legend, the reader is referred to the web version of this article.)

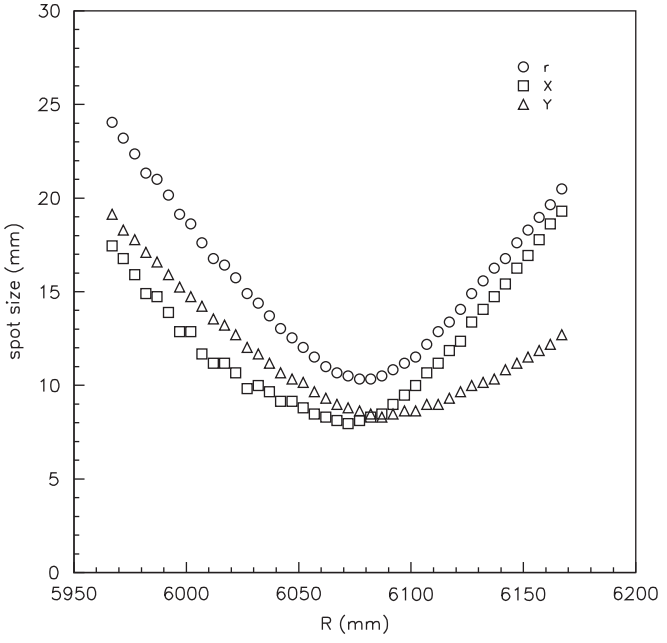

Fig. 12. Typical relation between spot size and distance from a mirror segment (circles: spot sizes; squares and triangles: projected spot sizes on X and Y axes, respectively).

in which 90% of the detected photons fall; this circle was centered at the weighted center of the image. Circles in Fig. 12 show an example relation between the spot size and the distance from a mirror. From the data points (circles) in Fig. 12, we obtain the curvature radius to be 6082 mm. Typically, as shown in Fig. 11, the image shape was a non-ideal circle, because the surface of the mirrors was slightly elliptical. This was caused by the limited accuracies of the ceramic model plates used in forming the mirror segments. Accordingly, we required an additional criterion for elliptical mirrors.

We also measured spot sizes to determine any elliptical component. First, we fitted a shot image at the beginning of a distance of 5967 mm with a line (called X axis), and another line (called Y axis) was obtained perpendicular to the X axis. These axes were fixed during the subsequent calculations. The shot image was projected onto these axes, and the projected spot sizes on these axes were calculated at each distance step of the stage away from the mirror. Finally, we obtained the curvature radii on these axes from the minima of these plots. We also required the curvature radii on the two axes to be within 6067 ± 100 mm. The projected spot sizes on the X and Y axes for the sampled mirror are shown as square and triangle points, respectively, in Fig. 12. From this figure, the curvature radii on the X and Y axes are 6072 mm and 6087 mm, respectively, and these radii also satisfy the above requirement. Fig. 13 shows the distribution of the curvature radius of the accepted mirrors, and Fig. 14 shows the distribution of the normal spot size in diameter at the curvature radius. The curvature radius of the accepted mirrors is 6057 mm (1σ : $+30/-20$ mm), and their spot size is 12 mm (1σ : $+3/-2$ mm) in diameter. Henceforth, 1σ indicates 68% confidence level.

From the acceptance test, we found that 5% mirror segments were unacceptable and additional segments were manufactured to reach the required number of acceptable segments.

3.4. Acceptance test for reflectance

We employed two different acceptance tests for the mirror segment reflectance. One is an accurate measurement in the laboratory for a wide wavelength range for sampled mirrors, which was performed by the manufacturer. The other is a simple measurement with a portable spectrophotometer for a narrow wavelength range for all the segment mirror.

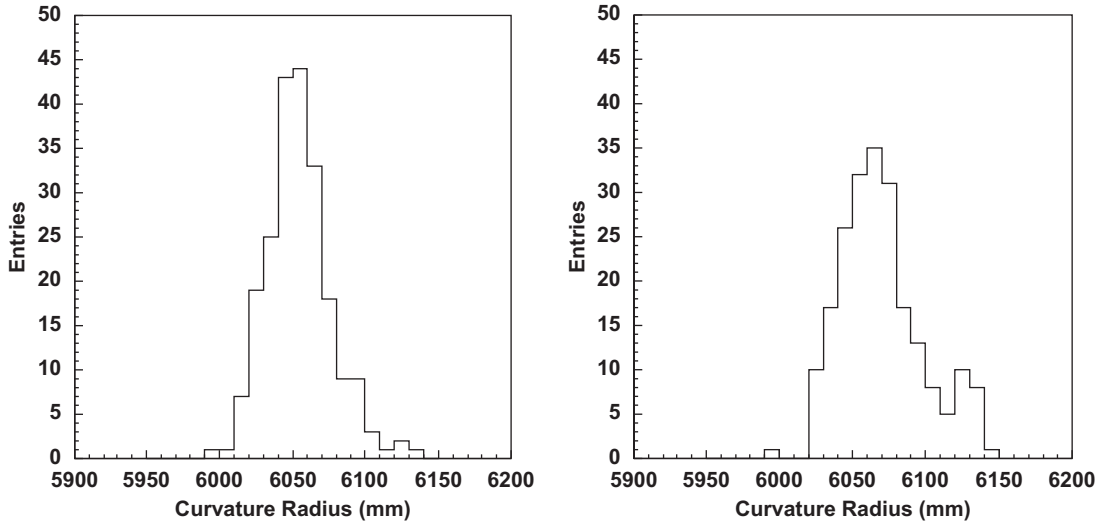

Fig. 13. Distribution of the curvature radius of mirror segments. Left: BRM (median: 6052 mm, 1σ: ± 20 mm), right: LR (median: 6067 mm, 1σ: $+30/-25$ mm).

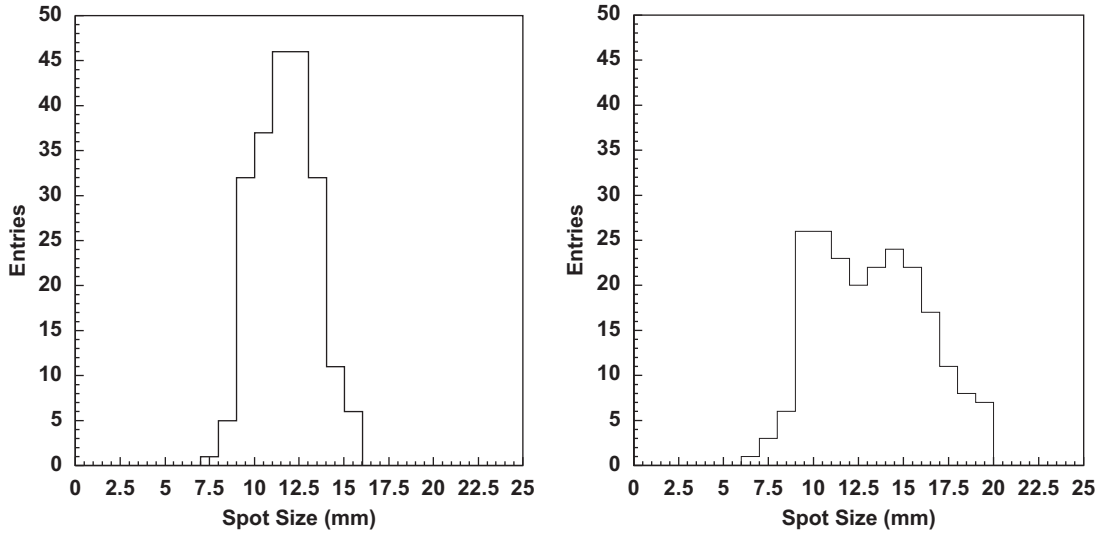

Fig. 14. Distribution of the spot size of mirror segments. Left: BRM (median: 11.7 mm, 1σ: ± 1.7 mm), right: LR (median: 13.2 mm, 1σ: ± 3.2 mm).

As it is difficult to measure the reflectance of the large curved segment mirrors accurately, the manufacturer also produced small flat test pieces of mirrors simultaneously with the sampled mirror segments and precisely measured the reflectance of the flat pieces as part of the delivery inspection process. The reflectance of the small flat mirrors was measured using a spectrometer (Jasco Inc., Ubest V-550), whose range, resolution, and accuracy are 190–900 nm, 2 nm, and 1%, respectively. Fig. 15 shows the typical reflectance of the sampled small flat test mirrors. This reflectance is more than 90% in the wavelength range of 300–400 nm, which contains all of the major air fluorescence lines.

Additionally, we used a portable spectrophotometer (Konica Minolta, Inc., CM-2500d) for acceptance inspections of all the manufactured mirror segments as well as for routine monitoring

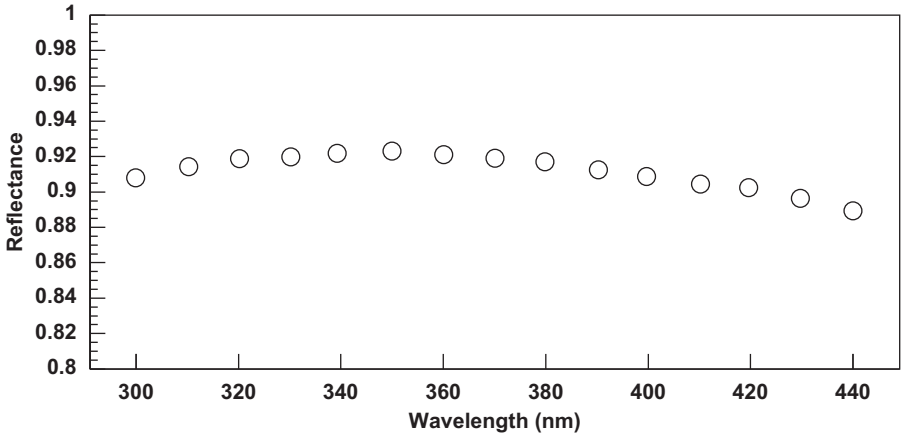

Fig. 15. Typical reflectance of a small flat test mirror shown as a function of wavelength, measured by the manufacturer using a spectrophotometer (Jasco Inc., Ubest V-550). Systematic error and measurement error are less than 1%.

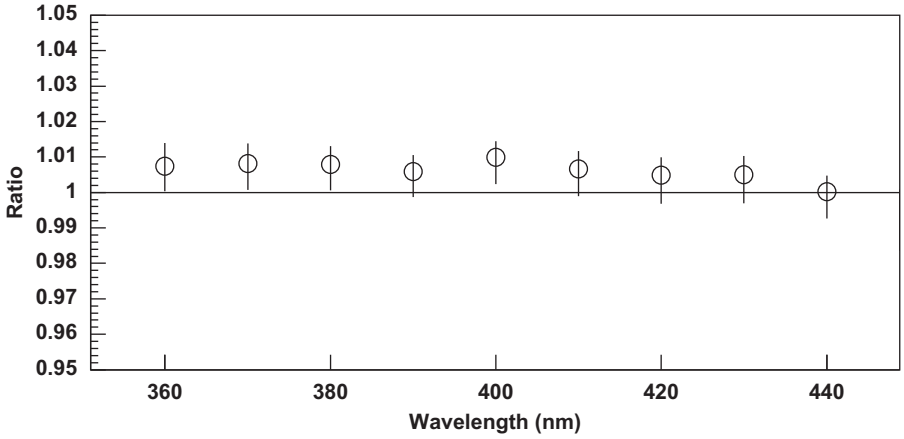

Fig. 16. A comparison of mirror reflectance between measurements using a portable spectrophotometer (Konica Minolta, Inc., CM-2500d) and a NIST measurement performed for an reference mirror (Ocean Optics Inc., STAN-SSH-NIST) shown as a function of wavelength (plots: our measurement value divided by the NIST one, error bars: 1σ).

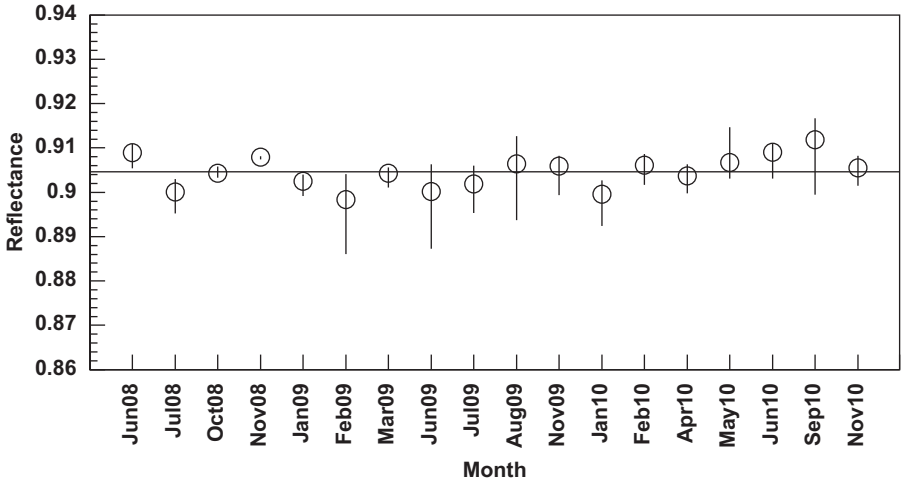

Fig. 17. Variation in the reflectance measurement of a reference mirror at 360 nm from June 2008 to November 2010 (plots: median value, error bars: 1σ, horizontal line: mean value of the plots).

of reflectance. The range and resolution of the spectrophotometer are 360–740 nm and 10 nm, respectively. The nominal uncertainties of measurement are less than 1%. To confirm its accuracy and stability, we measured the reflectance of a reference mirror 18 times in the period from June 2008 to November 2010. The reference mirror (Ocean Optics Inc., STAN-SSH-NIST) is quartz-coated; its reflectance was measured by the National Institute of Standards and Technology (NIST), USA. Fig. 16 shows a comparison between our measurements of the reference mirror and that performed by NIST. From this figure, the systematic differences are within $\pm 1\%$ and the deviations are within $\pm 1\%$ in the concerned wavelength range. Fig. 17 shows the variation in the reflectance of the reference mirror at the wavelength of 360 nm, measured using the portable spectrophotometer. The stability was 0.6% (1σ) during the period from June 2008 to November 2010.

The primary mirror for a FD is composed of 18 mirror segments. The median reflectance of the 24 primary mirrors as a function of wavelength is shown in Fig. 18. This figure shows that the reflectance in the wavelength range of 360–400 nm is greater than 90%. The distribution of the reflectance at 360 nm for all the mirror segment is shown in Fig. 19. This distribution shows that the differences in the reflectance depend on 108 random sampling points of each primary mirror (i.e. six points of each segment mirror) and that the variance is less than 1%, which is within measurement accuracies. Fig. 20 shows the reflectance of the primary mirrors in BRM and LR stations, which is the average of the 18 mirror segments, with 1σ error bars. All the FDs fulfilled the requirement that the averaged reflectance was greater than 90% at a wavelength of 360 nm.

4. FD installation

Mirrors and cameras were shipped from Japan to our observatory in Utah, USA, and these items were installed at BRM from February 2005 to July 2006 and at LR in March 2007. In this section, we describe the installations of the FDs and their alignment.

4.1. Installation of FD frame

As shown in Fig. 4, six FD frames were installed in each station (BRM and LR) with each frame supporting two FDs. Hence, in all, 12 FDs were installed in each station.

Each FD station building has three rolling doors to protect the FDs from sunlight, rain, wind, and other natural conditions. The FDs are directly exposed to air during FD observation, because no other protection windows were installed.

When the wind speed was greater than 15 m/s, the rolling doors were closed to prevent them from being stuck. In our design, we required less than 0.1° FOV deflections of the FD with wind speeds lower than 15 m/s. Wind-induced deflections of the FDs were studied by the manufacturer (Mitsui Engineering & Shipbuilding Co., Ltd.) using simulation programs and by applying wind-tunnel tests on a structure model of a station including FDs. From their studies, winds from the side of the FD building induce the maximum deflections in the FD frame. Because winds pass through the building from one door to another, their effective speed is not reduced by the building. However, the current design of the frame fulfills our requirement with regard to frame deflections, even in the worst wind condition.

To install the FD frames precisely, we conducted a survey and drew datum lines and points for FD geometry. Using a gyro-compass, the absolute azimuthal direction was measured with reference to a distant mountain peak. Uncertainties of the gyro-compass measurement was 0.017°, which was confirmed from

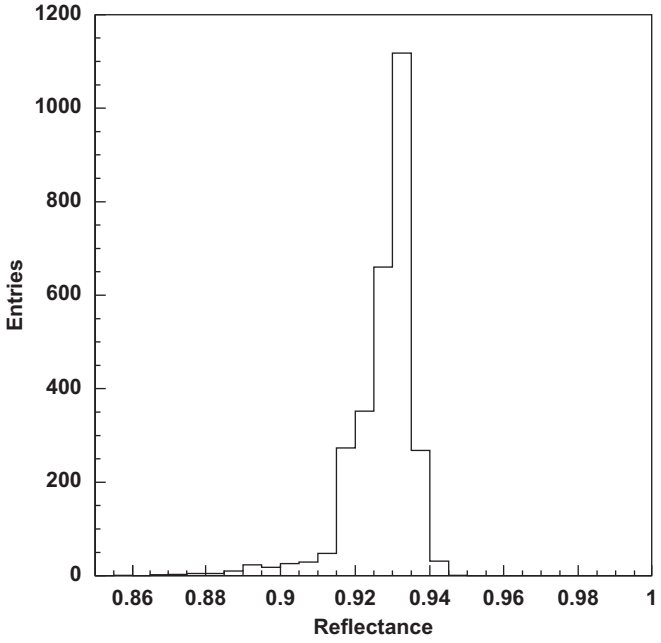

Fig. 19. Distribution of mirror reflectance of 24 primary mirrors (18 segments par each mirror, six measurement points par each segment, i.e. total number of measurement points is 2592) at 360 nm measured in March 2007 (median: 0.930, 1σ: $+0.004/-0.010$).

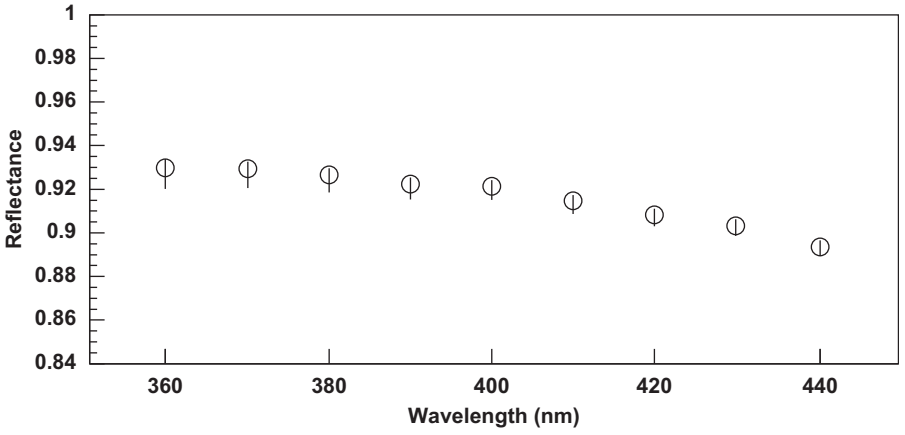

Fig. 18. Wavelength dependence of the reflectance of all mirror segments in March 2007 (plots: median value of 24 primary mirrors, error bars: 1σ).

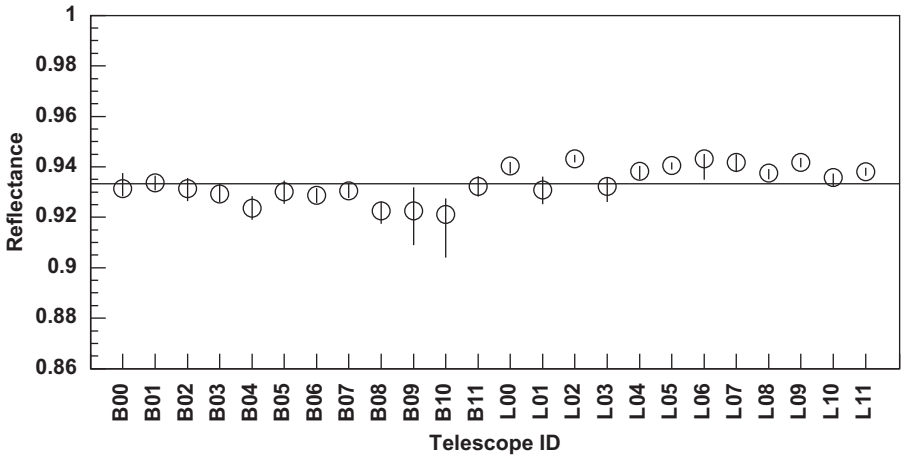

Fig. 20. Mirror reflectance at 360 nm (horizontal axis: telescope FD ID, B: BRM, L: LR, plots: median value of 18 mirror segments, error bars: 1σ, horizontal line: mean value of the plots).

the star observation using the gyro-compass. Three datum lines, shown as solid lines in Fig. 4, were drawn on the floor with relative accuracies of 0.017° between these lines. Azimuthal lines of each FD frame, shown as dashed lines in Fig. 4, were drawn from the datum lines with accuracies of 0.1° using a measuring tape. From the azimuthal lines, reference points for the FD frames were marked with accuracies of 1 mm.

We installed the FD frames, which can be separated into frames for cameras and mirrors, as shown in Fig. 3, in accordance with the following procedures. The FD frames were placed and fixed on the reference points, and before installing real cameras, a prototype standard camera was attached to the camera frames. This prototype standard camera had the same weight (167 kg), which includes the weight of PMTs and a camera box, and size of a real camera and was equipped with reference lines on the surface for adjusting positions. A steel cylinder with a diameter of 500 mm is mounted at the center of each primary mirror, as shown in Fig. 3. The central cylinder was used to adjust the alignment of mirror segments and the camera of the FD.

FD directions were adjusted by the following procedures. First, we installed a laser range meter on the central cylinder. Next, we adjusted the elevation angle to the specified value, monitored using a digital tilt meter (Digital Protractor, Pro 360), with an accuracy of $\pm 0.2°$. We adjusted the azimuthal angle of the cylinder for the central axis laser to point the string of a plumb 3000 mm away from the cylinder set exactly above the reference line on the floor. Next, the position of the camera frame was precisely adjusted with reference to the central axis laser. The upper limit for the installed error on the distance between the camera and the cylinder is ± 30 mm. If the distance error exceeded the upper limit, the camera frame was realigned. The misalignment within the upper limit was resolved when we installed mounts of mirror segments whose heights were adjusted to remove the distance error. To reduce the construction cost, we required relatively low accuracies on the elevation and rotation angle, which are within 1°. These uncertainties on the directions were confirmed with a star light analysis. On the other hand, this affects the negligible uncertainties of the effective area of the camera, the order of which is cos (1°). After the adjustment of the camera frame position, the prototype standard camera was unmounted from the camera frame.

After removal of the prototype camera, the positions of the mirror segment mounts were adjusted. Fig. 21 shows the schematic view of a jig called "BANANA1" for adjusting the positions of the mirror segment mounts. BANANA1 was mounted on the central cylinder of mirrors and can be rotated around the central axis of the cylinder. The equipment had two arms, one of which had three protruding legs of different lengths; the other arm had a counter weight. By rotating BANANA1, we adjusted the length of every mirror segment mount for one of the three legs on BANANA1 to be aligned with the reference point on the mount surface. At the same time, the pointing direction of each mirror segment was roughly adjusted using BANANA1.

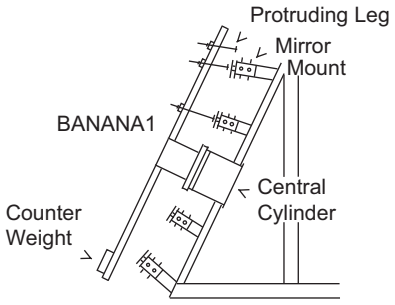

Fig. 21. Schematic view of the equipment called BANANA1 used for adjusting mirror segment mount. The equipment was mounted on the central cylinder of the mirror. By rotating the BANANA1, we adjusted the length of every mirror segment mount for one of the three legs on BANANA1 to be aligned with the reference point on the mount surface.

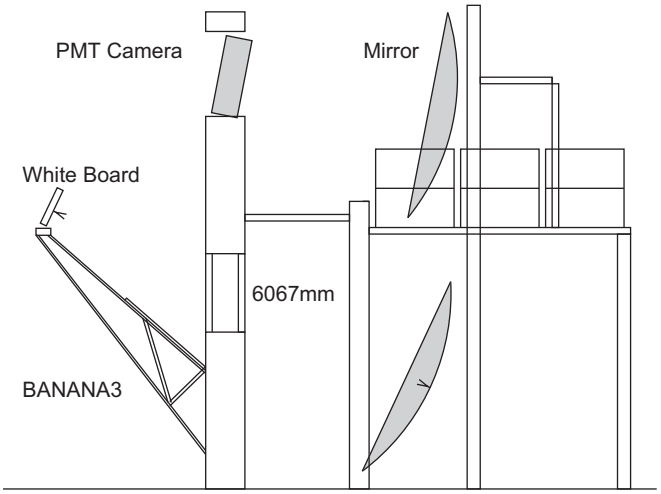

Fig. 22. Schematic view of the equipment for adjusting mirror segment pointing direction. The equipment is mounted on a camera support frame. A white board with LEDs is placed at a distance same as the mirror curvature radius of 6067 mm using this equipment.

4.2. Installation of cameras and mirrors

The cameras and mirrors were set on the FD frame by the following procedures. We set the mirror segments on their mounts and precisely aligned the pointing direction by screwing in and out two adjusting bolts on the mount. To adjust the direction of mirror segment, we use an equipment called "BANANA3", shown in Fig. 22. The equipment was mounted on the camera frame, and a small white board was perpendicularly set on the optical axis of the primary mirror. The distance between mirror segments and the white board was 6067 mm, which is the same distance as the nominal curvature radius of the mirrors. Green LEDs were mounted on the white board, 5−15 cm off of the optical axis, as shown in Fig. 23. When the direction of the mirror segment was adjusted, the LED lights were reflected to the symmetrical point across the optical axis. The direction was adjusted to an accuracy better than 0.1°, which was estimated from the accuracy of center position determination of reflected light of 5 mm (1/4 diameter of the reflected lights) and from the distance between mirror and the white board, 6067 mm. For parallel lights, this setting accuracy provided us the spots of 40 mm diameter, in which 68% of reflected photons fall, at the camera surface. After these adjustments, the mirror segment mounts were locked.

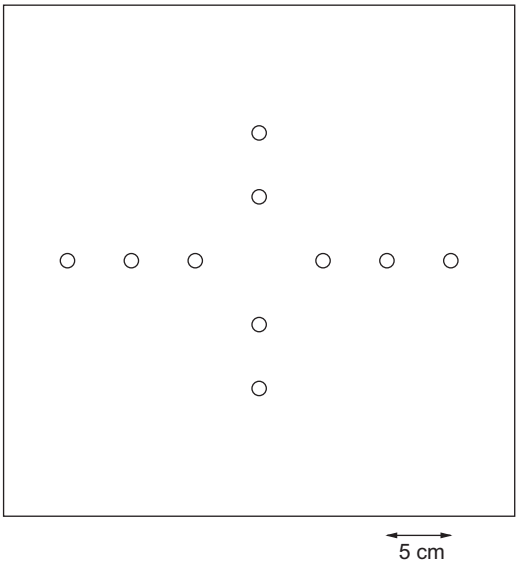

Fig. 23. Schematic view of the white board on the mirror alignment equipment called BANANA3 (circle: Green LED position).

The PMT cameras were mounted on the camera frames with an accuracy of 10 mm in the camera surface plane. This accuracy corresponds to ∼0.2° uncertainty of the FD's pointing direction. PMT cameras were then connected to signal, HV, and low voltage power cables. Finally, the wiring was confirmed through test operations.

The pointing directions of the FD are aligned to the designed values with better than 0.5° accuracies. These directions were confirmed by a star light analysis, which uses a similar method as in Ref. [11]. Our FDs record air fluorescence signals along with background photons (BGPs), as we employ a DC coupling for the PMT signal readout. Thus, we obtain the variations in BGP with a normal trigger rate of 2–3 Hz. When a star traverses the FOV of a PMT, the number of BGPs increases and decreases in a few minutes. The time variations of BGPs are simulated from star positions and FD directions. Using these estimated time variations of BGPs, we studied the FD directions and spot sizes of the primary mirror. If the FD directions and spot sizes are effected by nightly or seasonal temperature variations of optical setting, this star light analysis can provide a monitoring tool of these effects. From the analysis we obtained the true pointing directions of the telescope with an accuracy better than 0.1°. The correction values of the FOV direction of FD obtained from this study are used in our simulation and the EAS reconstruction programs. The star light analysis also provided measurement for spot sizes on the camera which include setting accuracies of mirror segments. Our results of the star light analysis will be reported in a future paper.

5. Mirror reflectance monitoring

The reflectance of the mirror segments is monitored every months. Fig. 24 shows the time variations of the averaged mirror reflectance at 360 nm of a typical lower FD (LR04). Mirror reflectance decreases with time, because our FDs are exposed to the air directly allowing dust to fall upon them and collect over time. In addition, the reflectance of lower mirrors decreases more rapidly than that of upper mirrors because they point more vertically.

To mitigate this effect, every summer, the mirrors are washed using purified water and detergent for sensitive equipment (Alconox, Inc., LIQUI-NOX). Purified water is obtained from tap water filtered

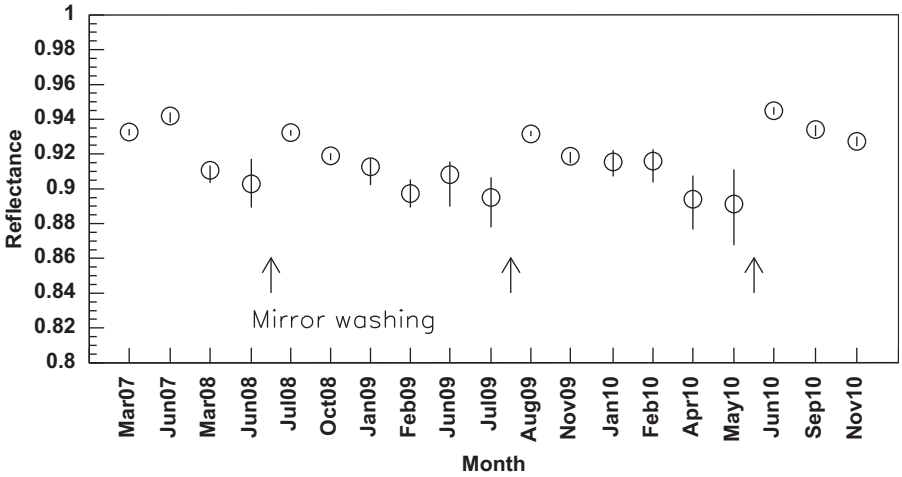

Fig. 24. Variation in the mirror reflectance at 360 nm of a typical lower FD (FOV: 17.5–33 in elevation) LR04 (plots: median value, error bars: 1σ). The mirror was washed after these measurements in July 2008, August 2009, and May 2010.

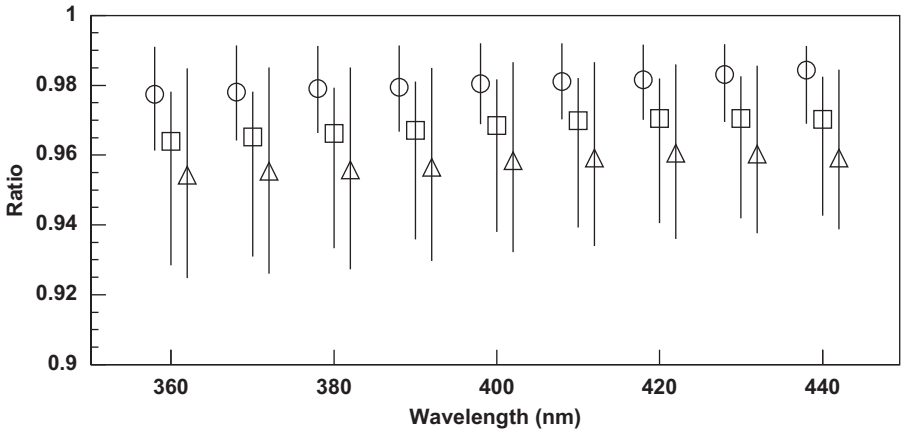

Fig. 25. Ratio of the measured mirror reflectance before and after washing (ratio: before/after) as a function of wavelength (plots: median value of 24 FDs, error bars: 1σ, circles: 2008, squares: 2009, triangles: 2010). These error bars show the non-uniformity of reflectance just before mirror washing. For visibility, the circles and triangles are slightly moved on the horizontal axis.

through charcoal and deionization filters. After washing, the mirrors are rinsed using purified water and dried naturally. Before and after mirror washing, mirror reflectance was measured. Fig. 24 shows that the reflectance of the mirror after washing is recovered to the same level as in the first installation. Fig. 25 shows the differences in mirror reflectance before and after washing at each wavelength; these differences have no clear wavelength dependencies.

In FD simulation and analysis, we use the monitor results of the mirror reflectance. Differences between continuous series of measurements cause systematic uncertainties of the mirror reflectance. The largest decrement of 4% occurred between June 2007 and March 2008 in Fig. 24. When we analyze the FD data in that period, we take this 4% as the systematic uncertainty of the mirror reflectance.

6. Summary

In Japan, we have produced PMT cameras and mirrors for use in the air fluorescence detector of the Telescope Array experiment. The cameras and mirrors that passed our acceptance inspections were shipped to our experimental site in Utah, USA. The FD frames, mirrors, and cameras were installed at the FD stations. The pointing directions of the FD are aligned to the designed values with an accuracy better than 0.5°, and the true directions have been obtained with the star light analysis (detailed description will be presented in a future paper). These true directions are used in our detector simulation and the EAS reconstruction programs. Monitoring of the performances of the cameras and mirrors is made according to the following schedules: the gains of PMT camera, hour by hour during FD operation, and mirror reflectance is monitored every few months. Our mirrors are washed every summer, and their reflectance after washing is recovered to the same level as in the first installation.

Acknowledgments

The Telescope Array experiment is supported by the Japan Society for the Promotion of Science through Grants-in-Aid for Scientific Research on Specially Promoted Research (21000002) "Extreme Phenomena in the Universe Explored by Highest Energy Cosmic Rays", and the Inter-University Research Program of the Institute for Cosmic Ray Research; by the U.S. National Science Foundation awards PHY-0307098, PHY-0601915, PHY-0703893, PHY-0758342, and PHY-0848320 (Utah) and PHY-0649681 (Rutgers); by the National Research Foundation of Korea (2006-0050031, 2007-0056005, 2007-0093860, 2010-0011378, 2010-0028071, R32-10130); by the Russian Academy of Sciences, RFBR Grants 10-02-01406a and 11-02-01528a (INR), IISN project No. 4.4509.10 and Belgian Science Policy under IUAP VI/11 (ULB). The foundations of Dr. Ezekiel R. and Edna Wattis Dumke, Willard L. Eccles, and the George S. and Dolores Dore Eccles all helped with generous donations. The State of Utah supported the project through its Economic Development Board, and the University of Utah through the Office of the Vice President for Research. The experimental site became available through the cooperation of the Utah School and Institutional Trust Lands Administration (SITLA), U.S. Bureau of Land Management and the U.S. Air Force. We also wish to thank the people and the officials of Millard County, Utah, for their steadfast and warm support. We gratefully acknowledge the contributions from the technical staffs of our home institutions and the University of Utah Center for High Performance Computing (CHPC). We thank HAMAMATSU Photonics K.K., Sanko Seikohjyo Co., Ltd., Quality Steel Fabricating And Welding, Inc., T&D Maintenance, Nitto Kogyo Corporation, and Mitsui Engineering & Shipbuilding Co., Ltd. for their kind support.

References

[1] H. Kawai, et al., Nuclear Physics B—Proceedings Supplements 175–176 (2008) 221.
[2] H. Kawai, et al., Journal of the Physical Society of Japan Supplement A 78 (2009) 108.
[3] T. Nonaka, et al., in: Proceedings of 30th International Cosmic Ray Conference, vol. 5, 2007, p. 1005 (submitted to Nuclear Instruments and Methods in Physics Research Section A, arXiv:1201.4964 [astro-ph.IM]).
[4] T. Abu-Zayyad, et al., Nuclear Instruments and Methods in Physics Research Section A 450 (2000) 253.
[5] J.N. Matthews, et al., in: Proceedings of 30th International Cosmic Ray Conference, vol. 5, 2007, p. 1157.
[6] H. Tokuno, et al., Nuclear Instruments and Methods in Physics Research Section A 601 (2009) 364.
[7] Y. Tsunesada for The Telescope Array Collaboration, in: Proceedings of 32nd International Cosmic Ray Conference (arXiv:1111.2507 [astro-ph.HE]).
[8] H. Tokuno, et al., Proceedings of 30th International Cosmic Ray Conference, vol. 5, 2007, p. 1013 (S. Kawana, et al., submitted to Nuclear Instruments and Methods in Physics Research Section A, arXiv:1202.1934 [astro-ph.IM]).
[9] Y. Tameda, et al., Nuclear Instruments and Methods in Physics Research Section A 609 (2009) 227.
[10] A. Taketa, et al., in: Proceedings of 29th International Cosmic Ray Conference, vol. 8, 2005, p. 209 (and now preparing a detailed paper).
[11] P.A. Sadowski, et al., Astroparticle Physics 18 (2002) 237.